HHS Public Access

Author manuscript

Nat Neurosci. Author manuscript; available in PMC 2018 February 14.

Published in final edited form as:

Nat Neurosci. 2017 October ; 20(10): 1361–1370. doi:10.1038/nn.4621.

Cerebellar Granule Cell Replenishment Post-Injury by Adaptive Reprogramming of Nestin+ Progenitors

Alexandre Wojcinski[1,*], **Andrew K. Lawton**[1], **N Sumru. Bayin**[1], **Zhimin Lao**[1], **Daniel N. Stephen**, and **Alexandra L. Joyner**[1,2,*]

[1]Developmental Biology Program, Sloan Kettering Institute, New York, NY, 10065

[2]Biochemistry, Cell and Molecular Biology Program, Weill Cornell Graduate School of Medical Sciences, New York, NY, 10065

Abstract

Regeneration of several organs involves adaptive reprogramming of progenitors, however, the intrinsic capacity of the developing brain to replenish lost cells remains largely unknown. In this study, we discovered that the developing cerebellum has unappreciated progenitor plasticity, since it undergoes near full growth and functional recovery following acute depletion of granule cells, the most plentiful neuron population in the brain. We demonstrate that following postnatal ablation of granule cell progenitors, *Nestin*-expressing progenitors (NEPs) specified during mid-embryogenesis to produce astroglia and interneurons, switch their fate and generate granule neurons in mice. Moreover, Hedgehog-signaling in two NEP populations is crucial not only for the compensatory replenishment of granule neurons but also to scale interneuron and astrocyte numbers. Thus we provide insights into the mechanisms underlying robustness of circuit formation in the cerebellum, and speculate that adaptive reprogramming of progenitors in other brain regions plays a greater role than appreciated in developmental regeneration.

Introduction

The intrinsic plasticity of cells *in vivo* that enables adaptive reprogramming plays an important role in many regeneration processes[1]. Although, the principles that apply have been uncovered in a few mammalian tissues, the repair capacity of the postnatal brain remains largely unknown[1]. Indeed, a critical alternative to stem cell therapies for complex brain structures like the folded cerebellum and cerebral cortex with an enormous surface area is to stimulate endogenous stem cells for repair. The cerebellum (CB), consisting of 80% of the neurons in the human brain[2] (60% in mouse[3]), is involved in higher reasoning

*Corresponding authors: joynera@mskcc.org and wojcinsa@mskcc.org.

Accession codes: RNA-Seq data is accessible at NCBI GEO database, accession GSE100941

Author Contributions: A.W. and A.L.J. conceived the project; A.W., A.K.L., N.S.B. and A.L.J. designed the research; A.W., A.K.L., N.S.B., Z.L and D.N.S. performed the experiments; A.W., A.K.L., N.S.B. and A.L.J. analyzed the data and all authors discussed the data; A.W. and A.L.J. wrote the manuscript with contributions from all authors.

Competing Financial Interests: The authors declare no competing financial interests.

via neural circuits that connect throughout the cerebral cortex[4–6]. Unlike other brain regions, the CB undergoes its major growth in the third trimester and infant stage in humans, primarily due to proliferation of granule cell precursors (GCPs)[7, 8]. Consequently, the CB is highly prone to injury in babies born prematurely, and more over cerebellar hypoplasia is the second highest risk factor for autism[9].

The CB, which develops from the anterior hindbrain, has two embryonic progenitor zones. The ventricular zone (VZ), which gives rise to all the inhibitory neurons, including Purkinje cells (PCs)[10], and the upper rhombic lip that produces all the excitatory neurons, including granule cells (GCs) [11–13]. In mice, *Atoh1*-expressing granule cell precursors (GCPs) migrate over the surface of the CB at embryonic day (E) 13.5–15.5 and proliferate in the external granule cell layer (EGL) until ~postnatal day (P) 15 in response to Sonic Hedgehog (SHH) secreted by Purkinje cells (PCs)[14–16]. Postmitotic GCPs migrate past the PCL to form the internal granule cell layer (IGL). Interestingly, the EGL was shown to be replenished following irradiation of the rat brain[17]. However, the extent of the ultimate cerebellar recovery, as well as the cell type that replenished the EGL was not identified.

During CB development, only PCs and embryonically born interneurons derive directly from the ventricular zone. Other interneurons and astroglia (astrocytes and Bergmann glia) are generated by ventricular zone-derived progenitors that proliferate after birth in the cerebellar cortex[18–22]. The cortical progenitors display traits of immature astrocytes and express neural stem cell (NSC) markers such as Nestin, SOX2 and TNC (referred to here as *Nestin*-expressing progenitors or NEPs), and are found in several locations (white matter, PCL and below the EGL[18, 23]). Interestingly, progenitors in the PCL produce only astroglia *in vivo*, whereas bipotent interneuron/astroglial progenitors reside in the white matter[24]. Thus, NEPs have several subpopulations with distinct characteristics, but expansion of all is regulated by SHH-signaling[18, 25].

There is increasing evidence in many organs that progenitors that normally are restricted to a particular fate have under appreciated plasticity following genetic manipulation or when cultured *in vitro*[26]. For example, *Ptf1a* mutant ventricular zone-derived cells can produce a small number of GCs[27, 28] and ectopic expression of ATOH1 converts ventricular zone cells to a rhombic lip lineage[29]. In culture, P3-7 cerebellar progenitors can form multipotent clonal neurospheres that include some granule cell-like cells[18, 30]. Collectively these data raise the question of whether cerebellar NEPs have a greater differentiation capacity *in vivo* than is seen during normal development, especially following injury.

Here we report the ability of the developing CB to almost fully recover after a major depletion of the perinatal EGL. Using multiple genetic approaches and live imaging of cerebellar slices, we conclude that NEPs in the PCL proliferate, migrate into the EGL, initiate *Atoh1*-expression, and produce GCs that incorporate into the IGL. Furthermore, white matter NEPs undergo a transient delay in interneuron and astrocyte generation. HH-signaling in NEPs is crucial for both recovery of the EGL and scaling of interneuron numbers after injury. We provide a striking example of the adaptive reprogramming capacity of brain progenitors, as well as raising the possibility that NEPs could be harnessed for therapeutic repair of the developing cerebellum.

Results

Minor adult cerebellar hypoplasia following GCP ablation

To determine the regenerative capacity of the newborn CB, we specifically irradiated the CB of P1 mice with a single dose of 4 G*y* (Fig. 1A–B). Histology and TUNEL assay at P2 revealed the high sensitivity of the EGL (PAX6+ layer) to irradiation-induced cell death, compared to cells in the cerebellar cortex (n=4, Fig. 1C,D,G,H and Fig. S1). Moreover, by P3 the EGL was greatly diminished and the CB smaller than control littermates (n=4, Fig. 1E,F,I,J). Nevertheless, by P30 irradiated (IR) mice (n=11) had a normal morphology and cytoarchitecture with only a small reduction in the size of the CB (mean=81.16% ± 0.07 % area of controls) and (Fig. 1K–M).

To test whether motor function in adults (5–6 week old) was disrupted after irradiation, we assessed two motor behavior paradigms, and confirmed normal grip strength in Non-IR (Normalized force=5.88±0.16) and IR (Normalized force=5.83±0.14) mice (n=18 for each condition) (Fig. 1N). Interestingly, no difference was observed in the performance on the accelerating rotarod of IR mice (259.5±7.12 sec) compared to Non-IR mice (245.5±8.49 sec) (Fig. 1O). In the footprint analysis, IR mice had only a slightly different stride length compared to Non-IR mice (Non-IR= 6.522±0.119 cm; IR= 6.214±0.067 cm)(Fig. 1P, R), with no significant difference in either sway (Non-IR= 2.474±0.051 cm; IR= 2.430±0.076 cm) or stance (Non-IR= 4.126±0.051 cm; IR= 3.979±0.054 cm) lengths (n=18 for each condition) (Fig. 1P, R), or in the ratio of R and L stance (% absolute [stance L – stance R]/ longest stance)(Non-IR= 5.77±0.82%; IR= 5.63±0.67%) (Fig. 1Q, R). All together, depletion of the mouse EGL at P1-3 is not sufficient to induce major long-term cerebellar hypoplasia or motor behavior defects, raising the possibility of a compensation mechanism in the developing CB after acute injury.

The EGL is replenished after injury

We next measured the area of midsagittal cerebellar sections at different stages, and found that the size of IR cerebella was reduced compared to Non-IR controls from P3 onwards (Fig. 1A), with a decrease in growth until P6 (~60% the area of controls at P6) and then a recovery phase (Fig. 2B). Interestingly, after P8 a similar growth curve was seen in both control and IR mice (Fig. 2A). Measurement of EGL thickness at P5 and P8 revealed that the EGL was progressively replenished (Fig. 2C,E,G,K,M). Furthermore, at both time points, the EGL contained a higher proportion of Ki67+ GCPs in the outer EGL compared to controls, suggesting an expansion of the newly forming EGL due to delayed differentiation (Fig. 2D,F,H,L,N). Curiously, we observed SOX2+ cells within both the molecular layer and EGL at P5, something not seen in controls (Fig. 2I,O). By P8, only EGL cells expressing a low level of SOX2 were observed in IR cerebella, with none in controls (Fig. 2J,P). Our results highlight an unexpected ability of the CB to partially recover after EGL injury.

NEPs do not normally produce GCPs/GCs *in vivo*

The SOX2 expression in the regenerating EGL lead us to hypothesize that NEPs contribute to the cellular compensation mechanism by changing their fate and migrating to the EGL. To test this idea, we validated two genetic tools: a *Nestin-FlpoER* transgene[31] to perform

Genetic Inducible Fate Mapping (GIFM)[32] of NEPs with Flippase (Flp)-dependent *R26*$^{FSF\text{-}cDNA}$ reporter alleles (FSF=Frt-Stop-Frt), and a *Nes-CFP* transgene[33] to observe NEP behaviors. Analysis of P1 *Nestin-FlpoER/+;R26*$^{FSF\text{-}TdTomato/+}$ (*Nes-TDTom*) mice administrated Tamoxifen (Tm) at P0 revealed that the initially marked cell population was SOX2+ (Fig. S2B) and doesn't express the GCP marker *Atoh1-Gfp* (n=3) (Fig. S2A). Consistent with GIFM using *Tnc*^{CreER} [18], in *Nestin-FlpoER/+;R26*$^{FSF\text{-}GFPCre/+}$ (*Nes-GFP*) mice at P8 51.37±3.97% of the GFP+ cells expressed the interneuron marker PAX2 and 37.24±6.59% the astrocyte and Bergmann glial marker S100β (30.43±5.84% S100β+/SOX2+ and 6.81±2.72% S100β+ only) and 7.75±2.36% expressed SOX2 only (n=3, Fig. S2C–F and also see Fig. S10). Importantly, the rare GFP+ cells located in the EGL (5.16±0.8% of total GFP+ cells, or ~27 cells per section per lobule 4/5) did not express PAX6 (n=3, Fig. S2D) and in fact, 91.15±3.87% of these cells expressed PAX2 and 1.5±2.12% S100β. In addition, no PAX6+/GFP+ cells were observed in the IGL, except in lobule 10, which was excluded from further analysis since GCPs cannot migrate between fissures[34]. As expected, 96.74±0.15% of Nes-CFP+ cells expressed SOX2 and 41.12±1.48% expressed the mature astroglial marker S100β (with 97.54±0.42% of Nes-CFP+ S100β+ cells also expressing SOX2) at P4 (n=3, Fig. S2G,H), and none expressed PAX6. Furthermore, at P3 only ~5 Nes-GFP+ cells were seen in the EGL of lobule 4/5 in non-irradiated mice per section, and only ~16 in irradiated mice, compared to ~3,000 [total] cells in the normal EGL (data not shown). Thus, we have effective tools to mark and fate map NEPs that normally generate interneurons and astroglia.

NEPs form multipotent neurospheres

We next tested whether Nes-CFP+ cells isolated by FACs from P4 cerebella (Fig. S3A,B) can form multipotent neurospheres in culture, and found these cells efficiently generate neurospheres expressing CFP and SOX2 within 7 days (n=3, Fig. S3C,D) at densities as low as 60 cells per well, whereas Nes-CFP- cells failed to form spheres even at densities of 6,000 cells per well (stem cell frequency = CFP+: 1/30.5 and CFP-: 1/22,500; Fig. S3E). Moreover, the Nes-CFP+ primary neuropheres gave rise to secondary and tertiary neurospheres, confirming their ability to undergo long-term self-renewal (Fig. S3F). Finally, neurospheres could differentiate into cells expressing neuronal (TuJ1), astroglial (GFAP) and oligodendrocytic (O4) markers (Fig. S3G–J), demonstrating their multipotency. Thus, NEPs in the postnatal CB represent NSCs.

NEPs switch their fate to become GCPs and produce GCs after EGL injury

We next performed *Nes*-GIFM following Tm administration at P0. CB area measurements revealed that, although Tm delayed recovery compared to untreated mice, the CB of IR *Nes-TDTom* mice progressively recovered and reached 74% ± 0.09% of the size of controls by P30 (n=7, Fig. 3A–D, Fig. S4). The foliation pattern and the cytoarchitecture of IR cerebella appeared grossly normal (Fig. 3A,B), although less so than in IR mice not given Tm. Significantly, and unlike Non-IR mice, we observed, not only a large increase in the number of *Nes*-derived TdTom+ cells in the IGL (3241±417 per mm^2 compared to 699.8±77.81 in Non-IR animals, n=3) but also that 60.63±2.26% were NeuN+ in IR mice and only 5.54±0.31% in Non-IR animals (Fig. 3E–H). Importantly, only in IR mice was the ML strongly positive for diffuse TdTom staining, indicating that most of the NeuN+ cells in the

IGL are GCs that project parallel fibers into the ML. Analysis at P5, P8 and P12 revealed a progressive increase in the number of *Nes*-derived cells in the EGL of IR mice (n=3, Fig. 3I–K,L–N,O). Interestingly, 35.66±13.2% of TDTom+ cells in the EGL expressed *Atoh1-GFP* at P8, with 80.63±3.24% of cells co-expressing TDTom at P12 (Fig. 3P). In contrast, in Non-IR mice ~10% of TDTom+ cells in the EGL (4±2.7 or 2.27±1.9 TDTom+ cells per section per lobule 4/5 at P8 or P12) expressed GFP at all stages (Fig. 3P). Importantly, the timing of TDTom+ cell accumulation in the EGL correlated with the maximum increase in growth (Fig. 3C,D). As with IR mice not administered Tm, we observed a progressive increase in the thickness of the EGL over time and higher proportion of proliferating cells compared to normal (Fig. 3Q). In addition, both the P12 and P16 EGL was thicker in the IR CB compared to controls, suggesting an extended period of GCP proliferation contributed to the recovery (Fig. 3K, N, Q and Fig. S5).

To validate the results we obtained using IR, we developed a second injury model specific to GCPs using Cre-inducible DTR (diphtheria toxin receptor) transgenic mice (iDTR). *Atoh1-tTA/+;TRE-Cre/+;R26*$^{LSL\text{-}DTR/+}$ triple transgenic mice were administered doxycycline from embryonic day (E)8.5 to E12.5 (*Atoh-DTR*)(Fig. S6A) to specifically target the EGL and avoid DTR expression in the cerebellar nuclei, as shown by DTR protein expression at P1 (Fig. S6B,C). TUNEL assay showed that EGL cells died upon DT administration (Fig. S6D,E). *Nes*-GIFM (*Nes-TDTom*) and analysis of Nes-CFP+ cell behavior in the model confirmed that TDTom+ cells populated the EGL by P6 (n=1) and CFP+ cells were present at P4 and P6 (n=2, Fig. S6F–K). Due to *Atoh1* transgene expression in respiratory neurons[35], the majority of mice died soon after P6. Our results demonstrate that using two different models of EGL depletion, NEPs change their fate, populate the EGL, turn on EGL genes (*Atoh1*, *Pax6*) and differentiate into GCs.

NEPs in the PCL contribute to recovery of the EGL

We next analyzed the behavior of NEPs using our *Nes-CFP* reporter mice. Interestingly, evaluation of the number of CFP+ cells per length of PCL revealed a significant increase at P4-6 in IR animals compared to controls (Fig. 4A,C,E). Consistent with this increase, the percentage of CFP+ cells that were Ki67+ in the PCL was significantly higher than in controls at P4 (Fig. 4F). Using a 1hr pulse of EdU, we found a significant increase in the proliferation index (% [Ki67+ GFP+ EdU+] cells of all [GFP+Ki67+] cells) of PCL NEPs at P3 compared to control (Fig. 4G). Interestingly by P6, the number of CFP+ cells in the PCL of IR mice was more comparable to controls and CFP+ cells had clearly begun populating the molecular layer and EGL (Fig. 4B,D,E and arrows/arrowheads in 4D′). Concomitantly, the percentage of Ki67+ CFP+ cells in the PCL was decreased, not only compared to P4 but also compared to P6 Non-IR controls (Fig. 4F). Finally, GFP protein continued to be detected in cells in the EGL at P8, although more weakly than at P6, and it was not detected at P12, indicating that as with SOX2 (Fig. 2O,P) expression of Nestin is extinguished once the NEPs enter the EGL (Fig. S7). In summary, our results suggest two phases of EGL recovery: increased proliferation of NEPs in the PCL, followed by migration into the EGL and recovery of normal NEP proliferation.

To test whether PCL NEPs replenish the injured EGL, we performed time-lapse imaging of P6 *Nes-CFP* cerebellar slice cultures from Non-IR and IR mice. Strikingly, by tracking the movement of individual cells during ~6hrs of imaging we observed Nes-CFP+ cells actively migrating from the PCL to the EGL in slices from IR but not control mice at P6 (Fig. 4H–K, and supp. videos 1–3). We also observed significantly more cells migrating from the molecular layer to the EGL in slices from IR mice compared to controls. Furthermore, highly motile CFP+ cells were present in the EGL of only IR CB slices (Fig. S8 and supp. videos 1, 2). Thus, NEPs located in the PCL expand and then migrate to replenish the EGL in response to a loss of GCPs.

White matter NEPs delay their production of interneurons and Astroglia during EGL recovery to maintain the proper scaling of cerebellar cell types

Since the proper function of the cerebellum depends on the proper scaling of the different cell types, we hypostatized that the production of interneurons and astroglia was reduced during EGL recovery. To test this idea, we analysed the behaviour of NEPs located in the white matter (WM) and IGL. Using live imaging, we did not observe any Nes-CFP+ cells in the IGL+WM region migrate to the EGL, although as expected a few cells in both IR and Non-IR slices migrated to the PCL and from the PCL to the ML where interneurons reside (Fig. 5A–C), suggesting that WM NEPs do not participate directly in EGL recovery.

Interestingly, we observed a trend towards a decrease in the percentage of Ki67+ NEPs in P4 WM+IGL of IR mice (21.33±1.76%) compared to non-IR controls (28±1.73%) (Fig. 5F). Consistent with this decrease, we found a significant decrease in the proliferation index of WM+IGL NEPs at P3 (Fig. 5D,E,G). However, this decrease was transient as the proliferation index progressively increased over time (29±1.73% at P3 and 42.67±1.45% at P6; p=0.0038) while staying constant in control animals (40.33±2.9% at P3 and 39±1.73% at P6; p=0.71) (Fig. 5G). In addition, there was a significant decrease in the density of CFP+ cells in the WM+IGL of P3 IR mice (Fig. 5H,J,P) followed by an increase in the number of CFP+ cells at P8 (Fig. 5H,K,Q), suggesting a delay in expansion of WM NEPs during initial EGL recovery. Indeed, there was a decrease in the density of NEP-derived PAX2+ interneuron progenitors in the WM+IGL at P4 but not P8 (Fig. 5I, L–M and R–S). Astrocyte density did not change, but the number must decrease because the CB is smaller (Fig. 5I, N–O and T–U). Thus, during recovery IGL+WM NEPs delay their expansion and production of interneurons and astroglia in order to maintain the proper scaling of cerebellar cell types.

SHH signaling plays a major role in NEPs for recovery after injury

RNA-Sequencing of FACS purified P5 Nes-CFP+ cells was performed to identify pathways involved in the two phases of recovery. As expected, the percentage of CFP+ cells of all cerebellar cells was significantly increased in IR cerebella (Non-IR: 5.26 ± 0.95% vs. IR: 12.63 ± 2.54%). 58 genes showed significant differences in expression (≥ 1.5-fold, adjusted p-value cutoff 0.05 and mean coverage of at least 15) (Fig. S9A and supp. Table 2). Pathway analysis identified 7 major categories of differentially expressed genes (Fig. S9B). As predicted, genes associated with cell cycle were markedly increased after IR, and cell adhesion and migration genes were down and up regulated, respectively (Fig. S9B).

Our RNA-seq data suggested that the HH target genes *Gli1*, *Ptch1* and *Ptch2* were slightly up regulated in IR NEPs (1.2, 1.4 and 1.7 fold change respectively with un-adjusted p-value <0.05)(supp. material). We validated this result by performing *in situ* hybridization (ISH) and found that *Gli1* expression was higher in the PCL of P5 IR cerebella compared to controls (Fig. S9C,E), but not at P8 when Nes-derived cells had populated the EGL (Fig. S9D,F). Furthermore, FACS isolated Nes-CFP+ cells from P4 and P6 IR and Non-IR cerebella showed a transient increase in *Gli1*, *Ptch1* and *Ptch2* expression after IR at P4 (Fig. S9G), suggesting a potential role for HH signaling in the recovery process. We first determined the effect of modulating HH-signaling in NEPs in normal development by ablating *Smoothened* (*Smo*) or overexpressing a constitutively active form of SMO (SmoM2) using our mosaic analysis (MASTR) technique[31] (Fig. 6A). *Nes-FlpoER/+;R26*$^{FSF\text{-}GFPcre/+}$*;Smo*$^{flox/flox}$ (*Nes-Smo* CKO) and *Nes-FlpoER/+;R26*$^{FSF\text{-}GFPcre/SmoM2\text{-}YFP}$ (*Nes-SmoM2*) mice or *Nes-GFP* controls (*Nes-FlpoER/+;R26*$^{FSF\text{-}GFPcre/+}$) were given Tm at P0, and the number of GFP+ cells quantified at P8 (Fig. 6B–E). Interestingly, we observed a reduction in the total number of GFP+ cells in the PCL and IGL+WM of *Nes-Smo* CKO cerebella compared to controls, but no change in the molecular layer and EGL. Furthermore, *Nes-Smo* CKO cerebella showed a decreased in the number of GFP+ SOX2+ (only) cells as well as *NEP*-derived PAX2+ interneurons and astroglia (S100β+ only or S100β+ SOX2+ cells) (n=3, Fig. S10A–B,D–E,G–J). In contrast, increasing the level of HH-signaling in NEPs led to an increase in the number of GFP+ *NEP*-derived cells located in the PCL but not elsewhere (Fig. 6D,E). Interestingly, whereas there was no difference in the number of GFP+ cells that expressed PAX2 in *Nes-SmoM2* cerebella compared to controls (except in the EGL) (n=6, Fig. S10C,H), elevated HH-signaling induced an increase in the production of *NEP*-derived astroglia in the PCL (Fig. S10F,I,J). Moreover, GFP+ NEPs with elevated SHH signaling entered the EGL at P8 (n=2/4) and at P12 (n=2/3), something not observed in *Nes-GFP* controls (Fig. S10K–P). *Nes-SmoM2* mice did not, however, develop cerebellar tumors (medulloblastomas) (n=0/9 >3 months).

We next tested whether the CB of *Nes-Smo* CKO mice have impaired recovery after irradiation at P1. Indeed, the CB of IR *Nes-Smo* CKO mice administered Tm at P0 recovered poorly and the CB reached only ~49% of Non-IR *Nes-GFP* size compared to ~74% for IR *Nes-GFP* (Fig. 6F–I–K). Importantly, no major cerebellar size reduction was observed in non-IR *Nes-Smo* CKO mice. Furthermore, no GFP+ cells were found in the EGL of IR *Nes-Smo* CKO mice at P12 (Fig. S11).

Behavior analysis revealed 5–6 week old IR *Nes-Smo* CKO mice had abnormal motor control (supp. videos 4–5). Although, forelimb grip strength measurements showed no significant difference between each cohort of mice, *Nes-Smo* CKO IR mice had significantly different stride (4.75±0.21 cm) and stance (3.26±0.1 cm) lengths compared to both *Nes-Smo* CKO Non-IR mice (stride=6.125±0.23 cm; stance=3.75±0.03 cm) and IR littermate control mice (stride=5.76±0.12 cm; stance=3.77±0.06 cm) (Fig. 6L, M). In addition, the percentage of stance difference was significantly higher in IR *Nes-Smo* CKO mice compared to other cohorts (Fig. 6N). Importantly, no significant difference was observed between Non-IR littermate control and *Nes-Smo* CKO Non-IR or IR littermate controls (Fig. 6L–N). Finally, we found that IR *Nes-Smo* CKO mice (181.9±12.47 sec) performed poorly on the

accelerating rotarod paradigm compared to both Non-IR littermate controls (236.6±17.18 sec) and *Nes-Smo* CKO non-IR (256.5±8.06 sec) mice (Fig. 6O). Moreover, we observed a trend towards a decrease in performance of IR *Nes-Smo* CKO mice compared to IR littermate controls, which performed more poorly than controls not given Tm (205.9±8.51 sec) (Fig. 6O). Thus, the CB recovers poorly after irradiation when HH-signaling is removed due to lack of expansion and migration of the NEP lineage to the EGL.

Discussion

There is emerging evidence in several organs for regenerative mechanisms that involve a change in identity, or adaptive reprogramming of normally lineage-restricted cells[1,26]. We have uncovered an extraordinary plasticity of cerebellar ventricular zone-derived committed progenitors *in vivo,* by their ability to switch their fate into the rhombic lip (granule cell) lineage after postnatal injury. Indeed, our data demonstrates that depletion of the EGL in neonates provides a potent environment for the expansion of PCL NEPs and their migration to and repopulation of the EGL. NEP-derived cells then lose their NSC markers (SOX2 and Nestin) and initiate expression of GC lineage-specific genes (*Atoh1*). The new GCPs proliferate before differentiating into GCs, and importantly have an extended proliferation phase compared to normal GCPs. *Atoh1* is specifically expressed in the proliferative outer EGL and is required for the generation of the EGL[36], in part through inducing the expression of the critical transcriptional activator in the SHH pathway, GLI2[37]. According to the important role of *Atoh1* in generating GCPs, we speculate that the migration of PCL NEPs into the EGL represents a crucial step in the acquisition of an excitatory phenotype. The postnatal EGL must maintain cues that allow the proper integration of new progenitors and enables recovery from severe injuries that would not be possible in a mature brain. Since rare cerebellar NSCs persistent in the adult[38], our study raises the possibility that given the right cues NEPs in the adult could be harnessed to contribute to cerebellar repair, and provides a rare example of adaptive reprogramming of committed progenitors to another normal state *in vivo* in mammals.

Although, our data clearly demonstrate the involvement of PCL NEPs to EGL regeneration, a population of NEPs located in the inner EGL could also participate in EGL recovery[23]. Using our *Nestin-CFP* and *Nestin-Flpo* transgenes we confirmed that a rare population of NEPs that express SOX2 reside in the inner EGL. Our fate mapping data showed that by P8, 91.15±3.87% of NEP-derived cells in the EGL express PAX2 and 1.5±2.12% S100β, suggesting that the initial population of NEPs in the P1 EGL is normally dedicated primarily to producing interneurons (Fig. 6,S10). Thus, if this subpopulation of NEPs is involved in EGL recovery after injury, it must be by adaptive reprogramming of EGL NEPs, similar to that of PCL NEPs.

Our live imaging data provide evidence that WM NEPs do not contribute to EGL replenishment after injury, as well as our finding that there is a transient decrease in the number of WM NEPs (Fig. 5). Furthermore, our RNA-seq data of all NEPs revealed that one of the top down regulated genes after IR is the immature interneuron gene *Pax2* (supp. material), one of the cell types generated by WM NEPs[18]. In addition, a small but nonsignificant decrease was observed for many astrocyte markers (e.g. *S100β* and *Gfap*; see

supp. material). Thus, our data indicate that the WM bipotent progenitors reduce their production phase in response to EGL loss. Importantly, interneuron production resumes by P8, a stage when the EGL has been replenished. Therefore, WM NEPs participate in the recovery, not by generating GCPs directly but by maintaining the scaling of the interneurons and glia during regeneration. Thus, two populations of NEPs are able to integrate proportional scaling of the numbers of several cerebellar cell types. Thus, there is a reset of the postnatal developmental clock of the CB after injury of the EGL to re-establish the correct proportions of cerebellar cell types (Fig. S12) to ensure normal cerebellar circuit formation.

We discovered that HH-signaling is both up-regulated in the PCL NEPs after injury and required for their expansion and migration to the EGL. Increasing HH signaling is also sufficient to induce migration of NEPs to the EGL. The polarized movement of NEPs indicates that there is a spatially organized factor that directs migration, possibly an attractant molecule produced by the pial surface of the CB. Although SHH has been described to act as a cellular chemoattractant[39, 40], since PCs are the only described source of SHH, it seems unlikely that SHH alone directs the migration trajectory of the NEPs toward the EGL.

The efficacy of the growth recovery following EGL depletion depends on the proper scaling of multiple cell types. Our demonstration that production of WM NEP-derived interneurons and astrocytes is transiently delayed during cerebellar recovery, suggests a very powerful cell-cell communication system exists that coordinates the response of the different NEP populations during recovery. Given that SHH regulates expansion of WM and PCL NEPs, and *Smo* is required in NEPs for cerebellar recovery, we propose that SHH is a critical component of the communication system via multi-directional signaling locally (to PCL NEPs) and through their dendrites (to the EGL) and axons (to WM NEPs). An attractive hypothesis is that PCs are able to sense a depleted EGL due to altered excitatory input because new GCs are not produced, and in response modulate the directionality of SHH signaling by concentrating the ligand locally in the PCL, inducing local expansion of NEPs, and possibly lowering its delivery through axons to WM NEPs, delaying expansion of WM NEPs and thus HH-dependent production of interneurons and astroglia (Fig. 5,S9). Thus one molecule (SHH) would direct the two NEP populations to have different acute responses to EGL depletion (Fig. S12) resulting in the proper scaling of cerebellar cell types. SHH is known to regulate regeneration in adult organs with progenitor populations that normally proliferate (e.g. skin) or can be stimulated to proliferate, such as the prostate[41]. In the adult brain we observed an increase in the number of cells in the PCL that express Nes-CFP after ablation of GCPs, but the cells did not proliferate or produce GCs (unpublished data). Our finding that increased HH signaling underlies proliferation and the fate change of NEPs provides a candidate pathway for reprograming NEPs to support regeneration after injury, stroke or neurodegeneration.

Since GCs are the most abundant cell type in the brain, the final size of the CB largely depends on the size of the EGL. Thus, migration of NEP-derived cells to the depleted EGL and their proliferation is a critical step in CB recovery, or catch-up growth, following irradiation. Catch-up growth has been divide into two subtypes: Type B, whereby the growth

phase is longer than normal with only a small or no increase in growth velocity compared to controls; and Type A, characterized by a growth velocity that exceeds the statistical limits of normality[42,43]. In our study, once the EGL was replenished at P6, the size of the CB progressively increased with a growth rate similar to that of control mice, fitting the definition of Type B catch-up growth. However, unlike the whole CB, recovery of the EGL followed Type A catch-up growth, with an increase in the thickness of the EGL and a boost in the proportion of proliferating cells in the EGL[43]. Furthermore, the EGL underwent an extended period of proliferation as in Type B catch-up growth. We speculate that growth recovery that involves both Type A and B, called Type C catch-up growth[43], is critical for effective recovery after injury to the CB, as the EGL must be replenished rapidly, and then a normal growth rate must ensue to maintain a cellular equilibrium in which the different cell types are produced in the correct proportions to ensure robust organ function.

In conclusion, the adaptive reprogramming capacity of NEPs and the signaling pathway (HH) we discovered provide critical insights for developing therapies to promote the intrinsic regenerative capacity of the CB. Our findings also raise the question of whether other regions of the brain have a greater developmental regenerative capacity than is appreciated.

Online Methods

Animals

The following mouse lines were used: *Nestin-FlpoER* and *Rosa26*$^{MASTR(frt\text{-}STOP\text{-}frt\text{-}GFPcre\ 46}$, *Atoh1-GFP*[47], *Nes-CFP*[48], *Rosa26*$^{FRT\text{-}STOP\text{-}FRT\text{-}TDTom}$ *(Jackson Laboratory, 021875), Atoh1-TtA (transgene to be described elsewhere), TetO-Cre*[49], *R26*^{iDTR} [50], *Smo*^{lox} [51] *and R26*$^{SmoM2\text{-}YFP}$ [52]. All mouse lines were maintained on an outbred Swiss Webster background and both sexes were used for the analysis. Animals were housed on a 12 h light/dark cycle and were given access to food and water *ad libitum*. All experiments were performed using young neonatal and adult animals (ages P1–P30) according to protocols approved by the Memorial Sloan-Kettering Cancer Center's Institutional Animal Care and Use Committee.

Newborn P1 mice were anesthetized by hypothermia and IR using an X-RAD 225Cx (Precision X-ray) Microirradiator in the MSKCC Small-Animal Imaging Core Facility. To specifically target the CB a 5mm diameter collimator was used and animals received a single dose of 4Gy from the left side.

Tamoxifen (Tm, Sigma-Aldrich) was dissolved in corn oil (Sigma-Aldrich) at 20mg/ml. *Nes-FlpoER/+; R26*$^{FSF\text{-}TDTom/+}$, *Nes-FlpoER/+; R26*$^{MASTR/+}$, *Nes-FlpoER/+; R26*$^{MASTR/+}$; *Smo*$^{lox/lox}$ and *Nes-FlpoER/+; R26*$^{MASTR/SmoM2\text{-}YFP}$ P0 mice received one 200μg/g dose of Tm via subcutaneous injection.

Doxycycline (Sigma) powder was dissolved in water to a concentration of 20 mg/mL. Pregnant females used to generate *Atoh1-TtA/+; TetO-Cre/+; R26*$^{iDTR/+}$ mice received Doxycycline at 0.02 mg/mL in drinking water from E8.5 to 12.5. DT was dissolved in PBS and P1 mice received one 30μg/g dose of DT via subcutaneous injection.

50 μg/g 5-ethynyl-2_-deoxyuridine (EdU; Invitrogen) was administered via intraperitoneal injection (10mg/ml in sterile saline) one hour before the animals were sacrificed.

Tissue Processing, Immunohistochemistry (IHC) and Transcript detection

For animals younger than P4, brains were dissected out and fixed in 4% paraformaldehyde overnight at 4°C. Animals P4-30 received 50 μl intraperitoneal injections of ketamine and received ice-cold PBS via transcardial perfusion followed by 4% paraformaldehyde. Brains were collected and submersion fixed in 4% paraformaldehyde overnight at 4°C. Tissues were processed for frozen embedding in optimal cutting temperature (OCT) compound and sectioned in parasagittal plan on a Leica cryostat at 12 μm. For IHC, sections were incubated overnight at 4C with the following primary antibodies: Rabbit anti-Ki67 (Thermo Scientific, RM-9106-S0), Mouse anti-P27 (BD Pharmigen, 610241), Rabbit anti-PAX6 (Millipore, AB2237), Goat anti-SOX2 (R&D System, AF2018), rabbit anti-GFP (Life Technologies, A11122), rat anti-GFP (Nacalai Tesque, 04404-84), rabbit anti-S100β (DAKO, Z0311), Rabbit anti-PAX2 (Invitrogen, 71600), Mouse anti-NeuN (Millipore, MAB377), Mouse anti-Tuj1 (Covance, MMS-435P), Mouse anti-O4 (Millipore, MAB345) and Goat anti-hHB-EGF (DTR detection) (R&D System, AF231) diluted in PBS with 5% BSA (Sigma-Aldrich) and 0.3% Triton X-100 (Fisher Scientific). Sections were then exposed for 2h at room temperature to secondary species-specific antibodies conjugated with the appropriate Alexa Fluor (1:500; Invitrogen). EdU was detected using a commercial kit (Life Technologies) after the IHC reactions. TUNEL staining and *in situ* hybridization were performed according to standard protocols. *Gli1* cDNA was used as the template for synthesizing digoxygenin-labeled riboprobes. Images were collected on a DM6000 Leica microscope and processed using Photoshop software.

Limiting Dilution Analysis and Serial Neurosphere Formation assay

FACS-isolated NesCFP+ and - cells were plated in three densities (60, 600 and 6,000 cells/well) in Ultra-low attachment 96-well plates (Corning) using Neurobasal media (Gibco, Life Technologies), supplemented with N2 (Gibco, Life Technologies), B27 (without vitamin A) (Gibco, Life Technologies), 20 ng/mL of human recombinant EGF (Gibco, Life Technologies) and 20 ng/ml FGF2 (Gibco, Life Technologies). Growth factors were supplemented every other day and the number of neurospheres was analyzed 7 days after plating. Frequency of stem cells was calculated as described previously[44]. For serial passaging, Neurospheres were dissociated every 7 days using Accutase (Innovative Cell Techonologies) and cells were replated at the original density (600 cells/well).

qRT-PCR Expression Analysis

RNA was isolated from FACS-isolated NesCFP+ cells using Qiagen miRNeasy Micro Kit (QIAGEN), using manufacturer's protocol. cDNA was prepared using iScript™ cDNA synthesis kit (Bio-Rad). qRT-PCR was performed using PowerUp Sybr Green Master Mix (Applied Biosystems). Fold changes in expression were calculated using the ΔΔCt method. The *GAPDH* gene was used to normalize the results. The following primer pairs were used: *Gli1*: F 5′CCAAGCCAACTTTATGTCAGGG3′ and R 5′ AGCCCGCTTCTTTGTTAATTTGA 3′; *Ptch1*: F 5′ AAAGAACTGCGGCAAGTTTTTG3′ and R 5′ CTTCTCCTATCTTCTGACGGGT 3′;

Ptch2: F 5′ CTCCGCACCTCATATCCTAGC 3′ and R 5′ TCCCAGGAAGAGCACTTTGC 3′

Live imaging

Ex vivo cerebellar slice culture was done as previously described[45]. Briefly, P6 cerebella were dissected in ice-cold complete Hanks Balance Salt Solution, embedded in 2.5% low-melting point agarose and saggitally sliced at 250μM using on a Vibratome. Slices were placed on millicell tissue culture inserts and immediately taken to either a Leica TCS SP8 or SP5 confocal microscope platform. Slices were maintained in Basal Medium Eagle with 2mM L-glutamine, 0.5% glucose, 50U/ml Penicillin-streptomycin, 1xB27 and 1xN2 supplements at 37°C and 5% CO_2. Image stacks were acquired every 3min for 5h 45min. Cell tracking was performed using Imaris software. The autoregressive tracking function was employed with a spot size of 6μM and a step size of 7μM. Manual correction was performed.

RNA-Seq

RNAs isolated from FACS-isolated NesCFP+ cells were sent to MSKCC Integrated Genomics Operation (IGO) core facility for sequencing. The output data (FASTQ files) were mapped to the target genome using the rnaStar aligner. Reads were mapped using HTSeq. Normalization of the full dataset and analysis of differential expression between sample groups were performed using the R/Bioconductor package DESeq. Heatmap was generated using the heatmap.2 function from the gplots R package. Gene Ontology was generated using DAVID Bioinformatics Resources 6.7 (https://david.ncifcrf.gov/).

Behavioral testing

Gait abnormalities were assessed using footprint analysis[53]. Both fore and hind feet were painted with red and blue or black nontoxic paint (Crayola), respectively before they walked on a strip of white paper along the floor of a 50 cm custom-made Plexiglas tunnel. The distances between hind limb footprints were measured to obtain “stride,” “sway,” and “stance” lengths. The measures were averaged for each mouse (3 run), and compared using Student’s t test. A total of 18 (10 males and 8 females) 5–6 weeks old WT mice (*Nes-CFP/+* and littlermates) were tested in both Non-IR and IR conditions. For *Nes-Smo* CKO experiment, 8 (5 females and 3 males) 5–6 weeks old IR *Nes-Smo* CKO and IR littermates control and 5 (4 females and 1 males) Non-IR *Nes-Smo* CKO and Non-IR littermates controls were tested.

The same groups of mice were also tested on an accelerating rotarod (model 47650; Ugo Basile), which was set to accelerate from 5 to 40 rpm over a period of 300 s. Each mouse was monitored for latency to fall (or three consecutive rotations if they gripped and rode around on the rod). Mice were tested using a paradigm of three trials per day, conducted on 3 consecutive days, with 10 min rest time given in their home cages between trials. Between-group differences were statistically evaluated by Student’s t test.

Mice had their fore limb grip strength tested using a force gauge (1027SM Grip Strength Meter with Single Sensor, Columbus Instruments). The mice were held up to the horizontal

grip and then were pulled steadily backwards until they could not hold on any longer. This was repeated 5 times per mouse, and the average force measurement was recorded. Force measurements were normalized to the mouse weight and expressed in Force/gm. Between-group differences were statistically evaluated by Student's t test.

Quantifications and Statistical Analyses

ImageJ software was used to measure the area (10^4 μm^2 or mm^2) of cerebellar section near the midline. For all IHC stainings, cell counts were obtained by using ImageJ and Neurolucida Software. For each developmental stage, three sections were analyzed per animal and ≥3 animals. Statistical analyses were performed using Prism software (GraphPad) and significance was determined at $P < 0.05$. All statistical analyses were one or two-tailed. For two-group comparisons with equal variance as determined by the *F*-test, an unpaired Student's *t* test was used. Welch's correction was used for unpaired *t*-tests of normally distributed data with unequal variance. P values and degrees of freedom are given in the figure legends. No statistical methods were used to predetermine the sample size, but our sample sizes are similar to those generally employed in the field. No randomization was used. Data collection and analysis were not performed blind to the conditions of the experiments. A Supplementary methods checklist and A Life Sciences Reporting Summary are available.

Data availability

The data that support the findings of this study are available from the corresponding authors upon reasonable request.

Supplementary Material

Refer to Web version on PubMed Central for supplementary material.

Acknowledgments

We thank Z.Yang for providing the *Nestin-CFP* line and for helpful discussions of unpublished data. We are grateful to B.Palikuqi (in S.Rafii's lab) for technical support with initial Nes-CFP FACS and R.Sillitoe, T.Stay and E.Lackey for their advice with performing the behavior tests. We thank K.Zaret for thoughtful comments on the manuscript, and past and present members of the laboratory for helpful discussions. We also thank the Flow Cytometry, Bio-informatics, Center for comparative medicine and pathology and Integrated Genomics Operation (IGO) core facilities of MSKCC for outstanding technical support. We also gratefully acknowledge P.Zanzonico for his help with mouse irradiation and B.Nieman for advice, and Q.Chen and the MSKCC Small-Animal Imaging Core Facility for technical services, and a Shared Resources Grant from the MSKCC Geoffrey Beene Cancer Research Center, which provided funding support for the purchase of the XRad 225Cx Microirradiator. This work was supported by grants from the Brain Tumor Center at MSKCC (to A.W.), National Brain Tumor Association (to A.L.J.) and NINDS (R01 NS092096 to A.L.J and F32 NS086163 to A.K.L.), and a National Cancer Institute Cancer Center Support Grant [P30 CA008748-48].

References

1. Jessen KR, Mirsky R, Arthur-Farraj P. The Role of Cell Plasticity in Tissue Repair: Adaptive Cellular Reprogramming. Dev Cell. 2015; 34:613–620. [PubMed: 26418293]
2. Azevedo FA, et al. Equal numbers of neuronal and nonneuronal cells make the human brain an isometrically scaled-up primate brain. J Comp Neurol. 2009; 513:532–541. [PubMed: 19226510]
3. Herculano-Houzel S, Mota B, Lent R. Cellular scaling rules for rodent brains. Proc Natl Acad Sci U S A. 2006; 103:12138–12143. [PubMed: 16880386]

4. Steinlin M. The cerebellum in cognitive processes: supporting studies in children. Cerebellum. 2007; 6:237–241. [PubMed: 17786820]
5. Tavano A, et al. Disorders of cognitive and affective development in cerebellar malformations. Brain. 2007
6. Fatemi SH, et al. Consensus paper: pathological role of the cerebellum in autism. Cerebellum. 2012; 11:777–807. [PubMed: 22370873]
7. Altman, J., Bayer, SA. Development of the cerebellar system in relation to its evolution, structure, and functions. CRC Press; Boca Raton: 1997.
8. Rakic P, Sidman RL. Histogenesis of cortical layers in human cerebellum, particularly the lamina dissecans. J Comp Neurol. 1970; 139:473–500. [PubMed: 4195699]
9. Wang SS, Kloth AD, Badura A. The cerebellum, sensitive periods, and autism. Neuron. 2014; 83:518–532. [PubMed: 25102558]
10. Hoshino M, et al. Ptf1a, a bHLH transcriptional gene, defines GABAergic neuronal fates in cerebellum. Neuron. 2005; 47:201–213. [PubMed: 16039563]
11. Wingate RJ, Hatten ME. The role of the rhombic lip in avian cerebellum development. Development. 1999; 126:4395–4404. [PubMed: 10498676]
12. Machold R, Fishell G. Math1 is expressed in temporally discrete pools of cerebellar rhombic-lip neural progenitors. Neuron. 2005; 48:17–24. [PubMed: 16202705]
13. Wang VY, Rose MF, Zoghbi HY. Math1 expression redefines the rhombic lip derivatives and reveals novel lineages within the brainstem and cerebellum. Neuron. 2005; 48:31–43. [PubMed: 16202707]
14. Sillitoe RV, Joyner AL. Morphology, molecular codes, and circuitry produce the three-dimensional complexity of the cerebellum. Annu Rev Cell Dev Biol. 2007; 23:549–577. [PubMed: 17506688]
15. Corrales JD, Blaess S, Mahoney EM, Joyner AL. The level of sonic hedgehog signaling regulates the complexity of cerebellar foliation. Development. 2006; 133:1811–1821. [PubMed: 16571625]
16. Lewis PM, Gritli-Linde A, Smeyne R, Kottmann A, McMahon AP. Sonic hedgehog signaling is required for expansion of granule neuron precursors and patterning of the mouse cerebellum. Dev Biol. 2004; 270:393–410. [PubMed: 15183722]
17. Altman J, Anderson WJ, Wright KA. Early Effects of X-Irradiation of the Cerebellum in Infant Rats: Decimation and Reconstitution of the External Granular layer. Experimental Neurology. 1969; 24:196–216. [PubMed: 5784132]
18. Fleming JT, et al. The Purkinje neuron acts as a central regulator of spatially and functionally distinct cerebellar precursors. Dev Cell. 2013; 27:278–292. [PubMed: 24229643]
19. Joyner, A., Sudarov, A. Genetic Neuroanatomy. In: Watson, C.Paxinos, G., Puelles, L., editors. The mouse nervous system. Academic Press; London: 2011.
20. Milosevic A, Goldman JE. Potential of progenitors from postnatal cerebellar neuroepithelium and white matter: lineage specified vs. multipotent fate. Mol Cell Neurosci. 2004; 26:342–353. [PubMed: 15207858]
21. Alexander T, Nolte C, Krumlauf R. Hox genes and segmentation of the hindbrain and axial skeleton. Annu Rev Cell Dev Biol. 2009; 25:431–456. [PubMed: 19575673]
22. Buffo A, Rossi F. Origin, lineage and function of cerebellar glia. Prog Neurobiol. 2013; 109:42–63. [PubMed: 23981535]
23. Li P, et al. A population of Nestin-expressing progenitors in the cerebellum exhibits increased tumorigenicity. Nat Neurosci. 2013; 16:1737–1744. [PubMed: 24141309]
24. Parmigiani E, et al. Heterogeneity and Bipotency of Astroglial-Like Cerebellar Progenitors along the Interneuron and Glial Lineages. J Neurosci. 2015; 35:7388–7402. [PubMed: 25972168]
25. De Luca A, et al. Exogenous sonic hedgehog modulates the pool of GABAergic interneurons during cerebellar development. Cerebellum. 2015; 14:72–85. [PubMed: 25245619]
26. Srivastava D, DeWitt N. In Vivo Cellular Reprogramming: The Next Generation. Cell. 2016; 166:1386–1396. [PubMed: 27610565]
27. Pascual M, et al. Cerebellar GABAergic progenitors adopt an external granule cell-like phenotype in the absence of Ptf1a transcription factor expression. Proceedings of the National Academy of Sciences of the United States of America. 2007; 104:5193–5198. [PubMed: 17360405]

28. Millen KJ, Steshina EY, Iskusnykh IY, Chizhikov VV. Transformation of the cerebellum into more ventral brainstem fates causes cerebellar agenesis in the absence of Ptf1a function. Proc Natl Acad Sci U S A. 2014; 111:E1777–1786. [PubMed: 24733890]
29. Yamada M, et al. Specification of spatial identities of cerebellar neuron progenitors by ptf1a and atoh1 for proper production of GABAergic and glutamatergic neurons. J Neurosci. 2014; 34:4786–4800. [PubMed: 24695699]
30. Lee A, et al. Isolation of neural stem cells from the postnatal cerebellum. Nat Neurosci. 2005; 8:723–729. [PubMed: 15908947]
31. Lao Z, Raju GP, Bai CB, Joyner AL. MASTR: a technique for mosaic mutant analysis with spatial and temporal control of recombination using conditional floxed alleles in mice. Cell reports. 2012; 2:386–396. [PubMed: 22884371]
32. Joyner AL, Zervas M. Genetic inducible fate mapping in mouse: establishing genetic lineages and defining genetic neuroanatomy in the nervous system. Dev Dyn. 2006; 235:2376–2385. [PubMed: 16871622]
33. Mignone JL, Kukekov V, Chiang AS, Steindler D, Enikolopov G. Neural stem and progenitor cells in nestin-GFP transgenic mice. The Journal of comparative neurology. 2004; 469:311–324. [PubMed: 14730584]
34. Legue E, Riedel E, Joyner AL. Clonal analysis reveals granule cell behaviors and compartmentalization that determine the folded morphology of the cerebellum. Development. 2015; 142:1661–1671. [PubMed: 25834018]
35. Huang WH, et al. Atoh1 governs the migration of postmitotic neurons that shape respiratory effectiveness at birth and chemoresponsiveness in adulthood. Neuron. 2012; 75:799–809. [PubMed: 22958821]
36. Ben-Arie N, et al. Math1 is essential for genesis of cerebellar granule neurons. Nature. 1997; 390:169–172. [PubMed: 9367153]
37. Flora A, Klisch TJ, Schuster G, Zoghbi HY. Deletion of Atoh1 disrupts Sonic Hedgehog signaling in the developing cerebellum and prevents medulloblastoma. Science. 2009; 326:1424–1427. [PubMed: 19965762]
38. Klein C, Butt SJ, Machold RP, Johnson JE, Fishell G. Cerebellum- and forebrain-derived stem cells possess intrinsic regional character. Development. 2005; 132:4497–4508. [PubMed: 16162650]
39. Angot E, et al. Chemoattractive Activity of Sonic Hedgehog in the Adult Subventricular Zone Modulates the Number of Neural Precursors Reaching the Olfactory Bulb. Stem Cells. 2008
40. Bijlsma MF, Borensztajn KS, Roelink H, Peppelenbosch MP, Spek CA. Sonic hedgehog induces transcription-independent cytoskeletal rearrangement and migration regulated by arachidonate metabolites. Cell Signal. 2007; 19:2596–2604. [PubMed: 17884337]
41. Petrova R, Joyner AL. Roles for Hedgehog signaling in adult organ homeostasis and repair. Development. 2014; 141:3445–3457. [PubMed: 25183867]
42. Williams JP. Catch-up growth. Journal of embryology and experimental morphology. 1981; 65(Suppl):89–101.
43. Boersma B, Wit JM. Catch-up growth. Endocr Rev. 1997; 18:646–661. [PubMed: 9331546]
44. Hu Y, Smyth GK. ELDA: extreme limiting dilution analysis for comparing depleted and enriched populations in stem cell and other assays. J Immunol Methods. 2009; 347:70–78. [PubMed: 19567251]
45. Famulski JK, et al. Siah regulation of Pard3A controls neuronal cell adhesion during germinal zone exit. Science. 2010; 330:1834–1838. [PubMed: 21109632]
46. Lao Z, Raju GP, Bai CB, Joyner AL. MASTR: a technique for mosaic mutant analysis with spatial and temporal control of recombination using conditional floxed alleles in mice. Cell reports. 2012; 2:386–396. [PubMed: 22884371]
47. Chen P, Johnson JE, Zoghbi HY, Segil N. The role of Math1 in inner ear development: Uncoupling the establishment of the sensory primordium from hair cell fate determination. Development. 2002; 129:2495–2505. [PubMed: 11973280]
48. Mignone JL, Kukekov V, Chiang AS, Steindler D, Enikolopov G. Neural stem and progenitor cells in nestin-GFP transgenic mice. The Journal of comparative neurology. 2004; 469:311–324. [PubMed: 14730584]

49. Perl AK, Wert SE, Nagy A, Lobe CG, Whitsett JA. Early restriction of peripheral and proximal cell lineages during formation of the lung. Proc Natl Acad Sci U S A. 2002; 99:10482–10487. [PubMed: 12145322]

50. Buch T, et al. A Cre-inducible diphtheria toxin receptor mediates cell lineage ablation after toxin administration. Nat Methods. 2005; 2:419–426. [PubMed: 15908920]

51. Long F, Zhang XM, Karp S, Yang Y, McMahon AP. Genetic manipulation of hedgehog signaling in the endochondral skeleton reveals a direct role in the regulation of chondrocyte proliferation. Development. 2001; 128:5099–5108. [PubMed: 11748145]

52. Mao J, et al. A novel somatic mouse model to survey tumorigenic potential applied to the Hedgehog pathway. Cancer Res. 2006; 66:10171–10178. [PubMed: 17047082]

53. Girirajan S, et al. How much is too much? Phenotypic consequences of Rai1 overexpression in mice. Eur J Hum Genet. 2008; 16:941–954. [PubMed: 18285828]

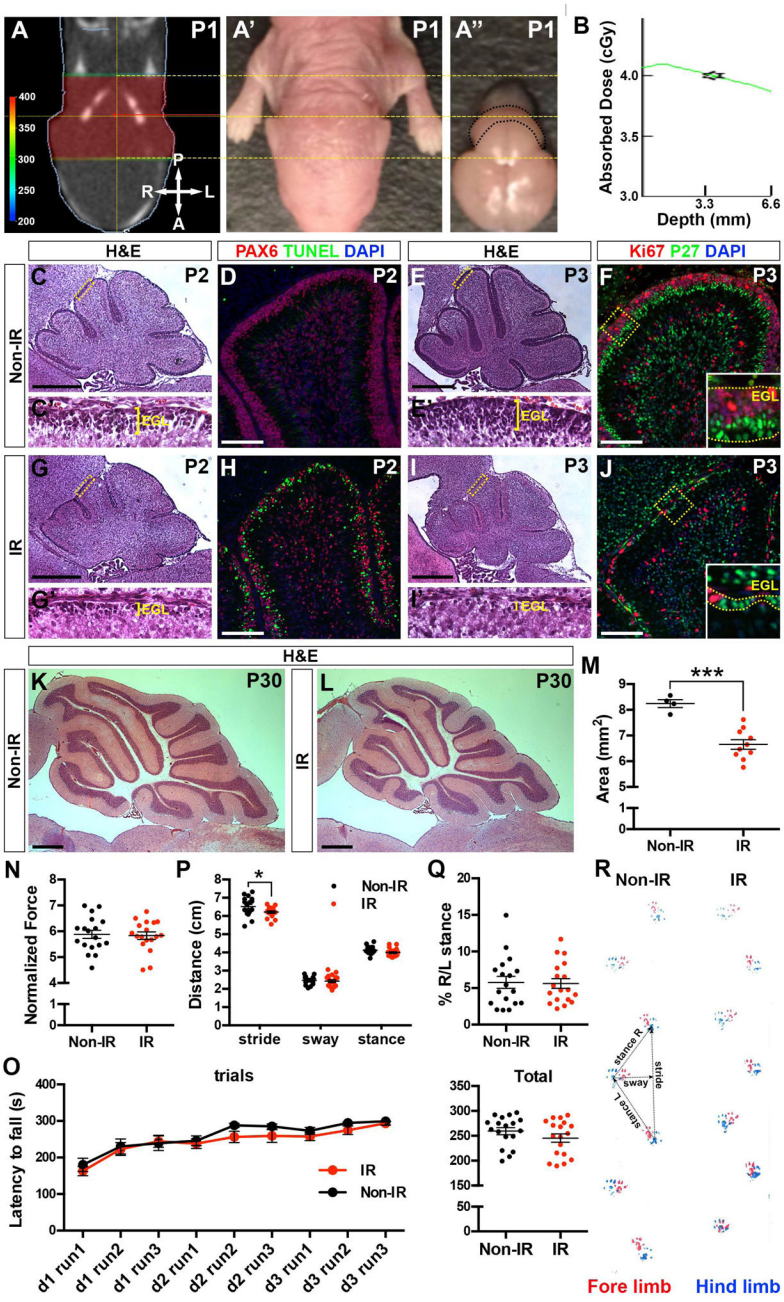

Fig. 1. Irradiation of cerebella at P1 results in a major loss of the EGL by P3 but growth largely recovers and motor behavior is intact at P30

(A) Dorsal view of a CT Scan **(A),** the whole head **(A′)** and the brain **(A″)** of P1 mice. Red in A represents the region irradiated. The dose color bar unit is cGY. Doted black line in A″ highlights the CB. **(B)** Dose volume histogram of absorbed dose across the whole tissue based on CT scan (coronal view) showing 4Gy dose is uniform across the tissue. **(C– L)** H&E and FIHC detection of the indicated proteins and dapi on midsagittal sections of Non-IR and IR mice at the indicated ages. IR induces cell death primarily in the EGL (TUNEL in **H**) and an almost complete loss of the EGL (yellow bracket/rectangle), indicated by

decreased cells that are proliferating (Ki67+) and differentiating (P27+). **D, F, H and J** are from lobule IV/V. Insets in **(F,J)** show high power images of the areas indicated by yellow rectangles. **(M)** Graph of the area of midsagital sections of P30 Non-IR (n=4) and IR (n=10) CB (p=0.0003, t(12)=5.053). **(N)** Graph representing fore limb grip strength expressed in normalized force between Non-IR (n=18) and IR (n=18) mice (p=0.811, t(34)=0.2414). **(O)** Graphs representing the latency to fall for each trial or total of Non-IR (n=18) and IR (n=18) mice. Statistics are provided in Supp. Table 1. **(P)** Graph representing stride (p=0.034, t(26.75)=2.238), sway (p=0.632, t(34)=0.484) and stance (p=0.056, t(34)=1.98) length between Non-IR (n=18) and IR (n=18) mice. **(Q)** Graph representing the percentage of right (R) and left (L) difference between Non-IR (n=18) and IR (n=18) mice (p=0.894, t(34)=0.1343). **(R)** Sample footprints (Forelimb in red and hind limb in blue) from Non-IR (n=18) and IR (n=18) mice. Dotted arrows represent stride, sway and stance. Graphical data are presented as means ± SEM and significance was determined with two-tailed Student's *t* test, $*P<0.05$ $***P<0.001$. Black and white scale bars indicate 500 and 100μm respectively.

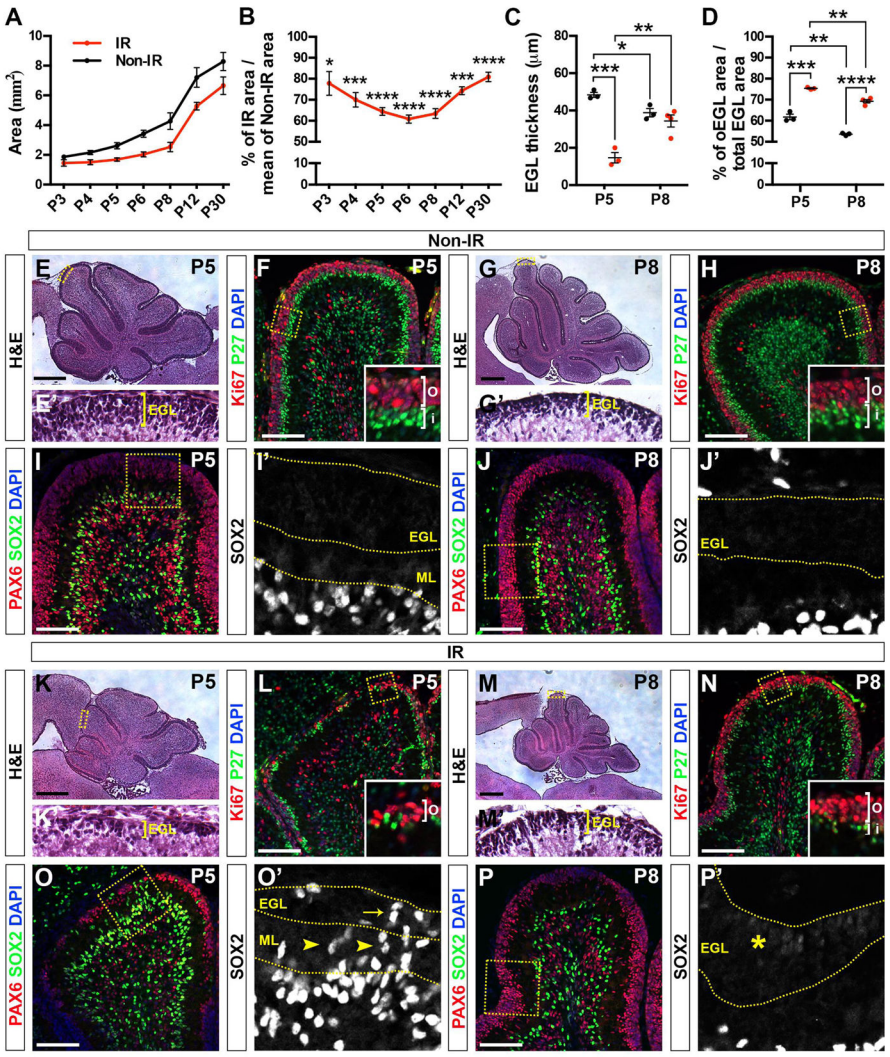

Fig. 2. The EGL is progressively replenished after injury

(A) Graph of the area of 3 midsagital sections of Non-IR (P3: n=2, P4: n=4, P5: n=4, P6: n=5, P8: n=6, P12: n=6 and P30: n=7) and IR (P3: n=4, P4: n=5, P5: n=5, P6: n=7, P8: n=6, P12: n=4 and P30: n=10) cerebella. **(B)** Graph showing the decrease in area of 3 midsagital sections as a percentage of Non-IR cerebella during development. **(C)** Graph of the EGL thickness expressed in µm perimeter of P5 and P8 Non-IR and IR cerebella (lobule IV/V was analyzed) (n=3). **(D)** Graph of the percentage of proliferative oEGL area over total EGL area of P5 and P8 Non-IR and IR cerebella (lobule IV/V was analyzed) (n=3 and P8 IR n=4). All of the analyses were performed on 3 midline sections per brain. Graphical data are presented as means ± SEM and significance determined with two-tailed Student's *t* test, **** *P<0.0001*, *** *P*<0.001, ** *P*<0.01 * *P*<0.05. Statistics are provided in Supp. Table 1. **(E–P)** H&E and FIHC detection of the indicated proteins and dapi on midsagittal cerebellar sections at the indicated ages. High power images are shown of the areas indicated by yellow rectangles (**′ and inset in F, H, L and N)**. EGL is indicated by yellow bracket in **E′, G′, K′** and **M′**. Proliferative Ki67+ outer (o) and post-mitotic P27+ inner (i) EGL are indicated by white brackets in **F, H, L** and **N**. Molecular layer (ML) and EGL are delimited by yellow

dotted lines in **I′, J′, O′** and **P′**. Arrowheads and arrow in **O′** indicate SOX2+ cells present in the ML and EGL respectively. Asterisks in **P′** indicate SOX2 low cells in the EGL. Black and white scale bars indicate 500 and 100μm respectively.

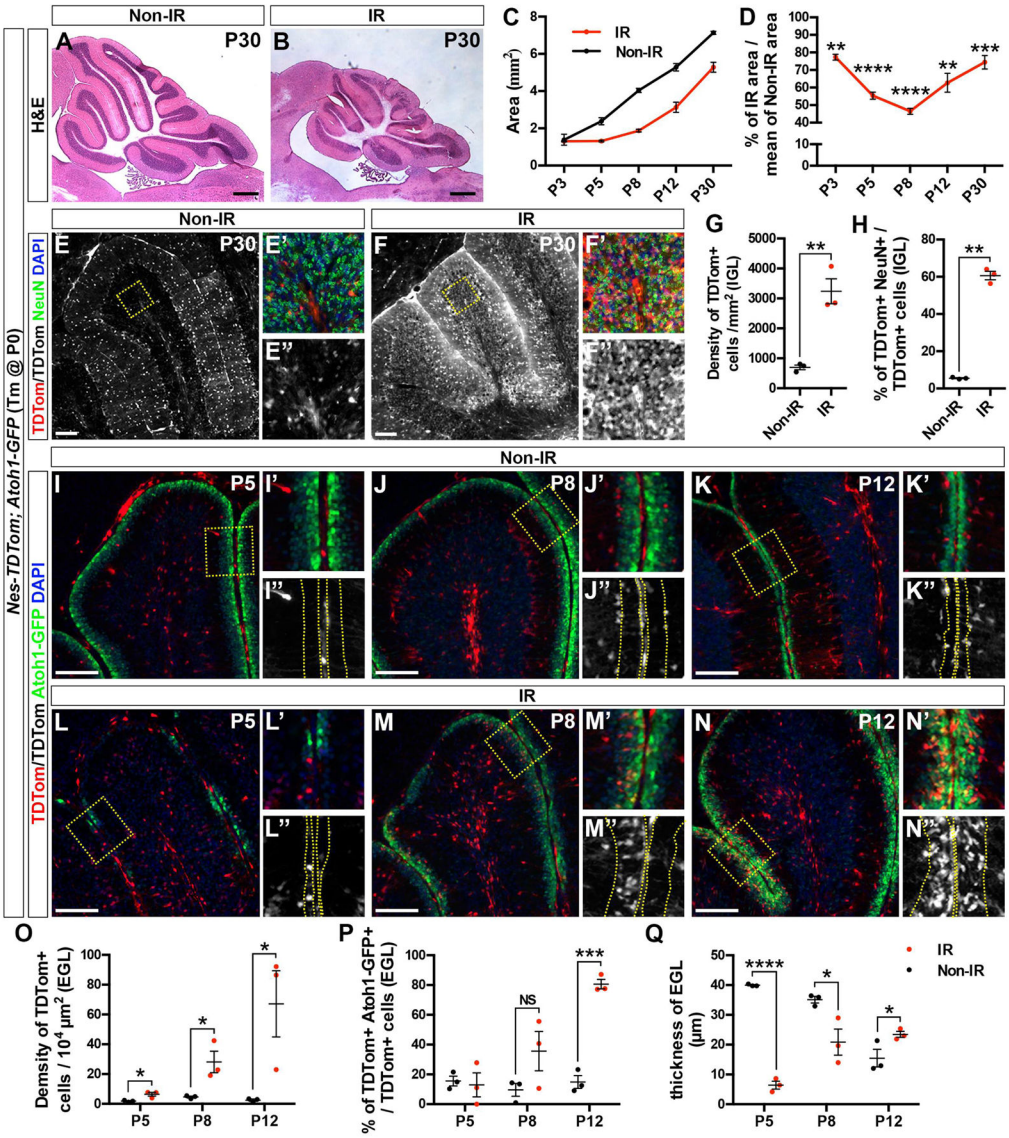

Fig. 3. NEPs populate the EGL and generate granule cells and rescue growth

(A and B) H&E of sagittal sections of the vermis of P30 Non-IR **(A)** and IR **(B)** *Nes-FlpoER/+; R26*$^{FSF\text{-}TDTom/+}$*; Atoh1-GFP/+* mice *(Nes-TDTom; Atoh1-GFP)* injected with Tm at P0. **(C)** Graph of the area of 3 midsagital sections of Non-IR (P3: n=2, P5: n=3, P8: n=4, P12: n=3 and P30: n=4) and IR (P3: n=3, P5: n=5, P8: n=6, P12: n=4 and P30: n=7) cerebella. **(D)** Graph showing the decrease in the area of 3 midsagital sections as a percentage of Non-IR cerebella during development (P3: p=0.0054, t(2)=13.6; P5: p<0.0001, t(4)=22.7; P8: p<0.0001, t(5)=32.07; P12: p=0.006, t(3)=7.011; P30: p=0.0005, t(6)=6.734). **(E–F)** FIHC detection of the indicated proteins and dapi on midsagittal cerebellar sections at P30. High power images are shown of the areas indicated by yellow rectangles. **(G)** Graph of the density of TDTom+ cells per mm^2 of P30 IGL in Non-IR and IR cerebella (lobule IV/V was analyzed) (n=3, p=0.0039, t(4)=5.985). **(H)** Graph of the percentage of TDTom+ cells that expressed the neuronal marker NeuN in P30 IGL Non-IR

versus IR cerebella (lobule IV/V was analyzed) (n=3, p=0.0014, t(2.075)=24.16). **(I–N)** FIHC detection of the indicated proteins and dapi on midsagittal cerebellar sections at the indicated ages. High power images are shown of the areas indicated by yellow rectangles and EGL is delimited by yellow doted line **(′** and **″). (O)** Graph of the change in density of TDTom+ cells per 10^4 μm^2 of P5, P8 and P12 EGL in Non-IR and IR cerebella (lobule IV/V was analyzed) (n=3, P5: p=0.025, t(4)=3.51; P8: p=0.016, t(4)=3.248; P12: p=0.022, t(4)=2.914). **(P)** Graph of the percentage of TDTom+ cells that expressed Atoh1-GFP in P5, P8 and P12 Non-IR and IR EGL (lobule IV/V was analyzed) (n=3, P5: p=0.778, t(4)=0.302; P8: p=0.135, t(4)=1.871; P12: p=0.0003, t(4)=12.24). **(Q)** Graph of the EGL thickness expressed in μm of P5, P8 and P12 Non-IR and IR cerebella (lobule IV/V was analyzed) (n=3, P5: p=0.012, t(2.101)=25.61; P8: p=0.017, t(4)=3.16; P12: p=0.031, t(4)=2.561). All of the analyses were performed on 3 midline sections per brain. All graphical data are presented as means ± SEM and the significance was determined with one **(O,Q)** or two-tailed Student's *t* test, ****$P<0.0001$, ***$P<0.001$, *$P<0.05$. Black and white scale bars indicate 500 and 100μm respectively.

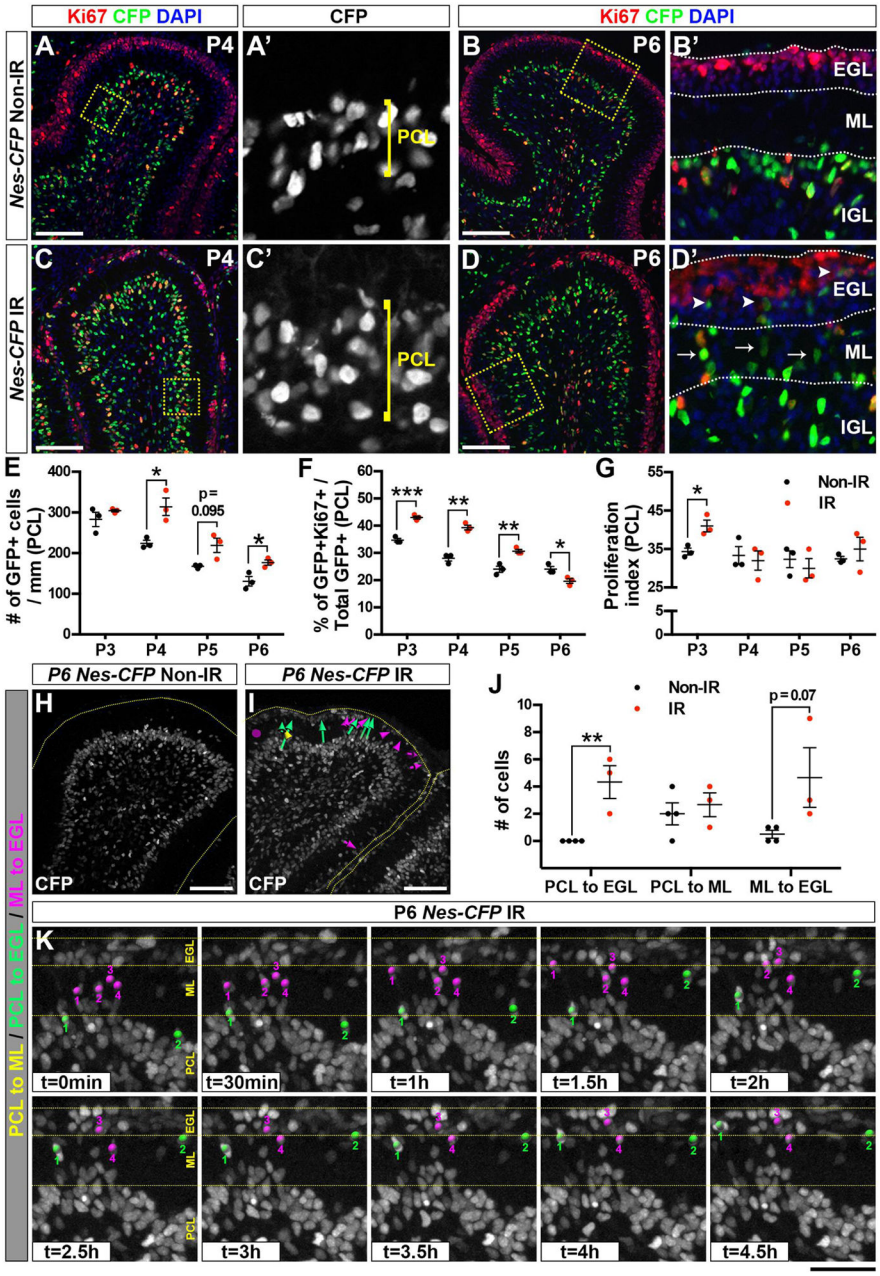

Fig. 4. PCL NEPs expand and migrate into the EGL after injury

(A–D) FIHC detection of the indicated proteins and dapi on sagittal sections of the vermis (lobule IV/V) of *Nes-CFP/+*mice. High power images are shown of the areas indicated by yellow rectangles **(′).** Purkinje cell layer (PCL) is indicated by yellow brackets **(A′ and C′)** and EGL, molecular layer (ML) and internal granule layer (IGL) by white lines **(B′ and D′)**. Arrow and arrowheads in **D′** indicate CFP+ cells present in the ML and EGL, respectively. **(E–G)** Graphs showing the changes in the numbers of CFP+ cells per mm length of PCL (n=3; P3: p=0.298, t(4)=1.195; P4: p=0.0173, t(4)=3.917; P5: p=0.095, t(2.099)=2.908; P6: p=0.0268, t(4)=3.418) **(E),** the proportion of proliferating (Ki67+) CFP + cells (n=3; P3: p=0.0007, t(4)=9.449; P4: p=0.0011, t(4)=8.5; P5: p=0.0075, t(4)=5; P6:

p=0.0314, t(4)=3.25) **(F),** and the proliferation index (% [Ki67+ GFP+ EdU+] cells of all [GFP+Ki67+] cells) (n=3; P3: p=0.019, t(4)=3.78; P4: p=0.717, t(4)=0.3885; P5: p=0.523, t(4)=0.7; P6: p=0.457, t(4)=0.8221) **(G)** at the indicated ages. All of the analyses were performed on 3 midline sections per brain and lobule IV/V was analyzed. **(H–I)** Detection of native CFP fluorescence on sagittal slices of the vermis (lobule IV/V) of P6 Non-IR **(H)** and IR **(I)** *Nes-CFP/+* mice showing displacement of CFP+ cells from the PCL or ML during 5h45min of imaging. Arrow color code is as indicated. **(J)** Graph change in the number of CFP+ cells crossing the indicated layers during imaging (Non-IR: n=4 and IR: n=3) (PCL to EGL: p=0.0076, t(5)=4.309; PCL to ML: p=0.6070, t(5)=0.5484; ML to EGL: p=0.0752, t(5)=2.240). All graphical data are presented as means ± SEM and significance were determined using two-tailed Student's *t* test, ***$P<0.001$, **$P<0.01$, *$P<0.05$. **(K)** Close-up images showing time laps images of movement of CFP+ cells. Color code for dots as indicated; number indicates individual cells. EGL and ML are indicated by yellow dotted lines. White and black scale bars indicate 100 and 50 μm respectively.

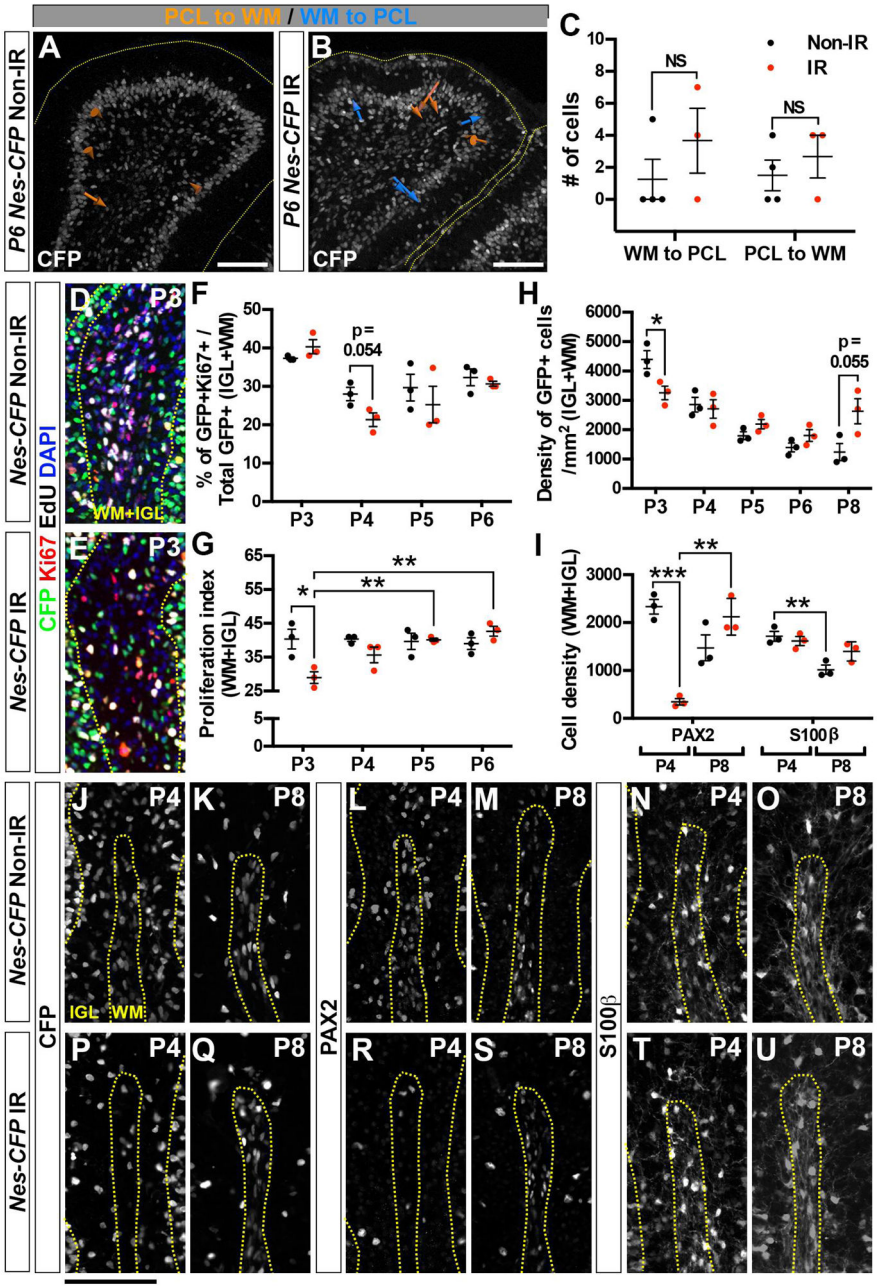

Fig. 5. WM NEPs delay their expansion and production of interneurons and astroglia

(A–B) Detection of native CFP fluorescence on sagittal slices of the vermis (lobule IV/V) of P6 Non-IR **(A)** and IR **(B)** *Nes-CFP/+* mice showing displacement of CFP+ cells to or from the WM during 5h45min of imaging. Arrow color code is as indicated. **(C)** Graph of the number of CFP+ cells crossing the indicated layers during imaging (Non-IR: n=4 and IR: n=3). **(D–E)** FIHC detection of the indicated proteins, EdU and dapi on sagittal sections of the vermis (lobule IV/V) of P3 *Nes-CFP/+*mice. WM + IGL are delimited by yellow dotted lines. **(F–I)** Graphs of the proportion of proliferating (Ki67+) CFP+ cells in WM+IGL (n=3) **(F)**, the proliferation index (% [Ki67+ GFP+ EdU+] cells of all [GFP+Ki67+] cells) (n=3)

(G), the density of CFP+ cells (n=3) **(H)** and PAX2+ interneurons (n=3) and S100β+ astrocytes (n=3) **(I)** per mm^2 of WM+IGL at the indicated stages. All of the analyses were performed on 3 midline sections per brain and lobule IV/V was analyzed. All graphical data are presented as means ± SEM and significance determined using two-tailed Student's *t* test, ***$P<0.001$, **$P<0.01$, *$P<0.05$. Statistics are provided in Supp. Table 1. **(J–U)** FIHC detection of the indicated proteins and dapi on sagittal sections of the vermis (lobule IV/V) of *Nes-CFP/+* mice at the indicated ages. WM + IGL are delimited by yellow dotted lines. Scale bars indicate 100μm.

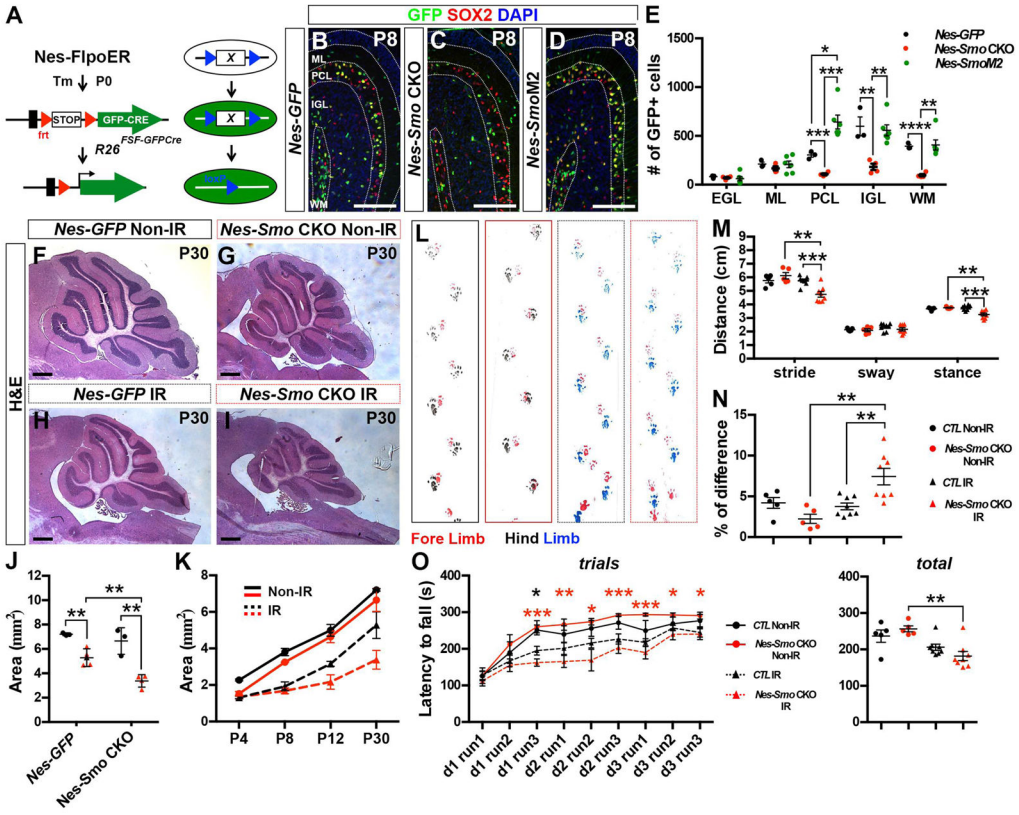

Fig. 6. HH signaling is required for NEPs to expand and populate the EGL and for substantial recovery of the cerebellum

(A) Schematic representation of the MASTR mosaic mutant approach. **(B–D)** FIHC detection of the indicated proteins and dapi on midsagittal sections (lobule VIII) of P8 *Nes-FlpoER/+; R26*$^{MASTR/+}$ (*Nes-GFP*, n=3, **B**) or *Nes-FlpoER/+; R26*$^{MASTR/+}$*; Smo*$^{lox/lox}$ (*Nes-Smo* CKO, n=4, **C**) or *Nes-FlpoER/+; R26*$^{MASTR/SmoM2\text{-}YPF}$ (*Nes-SmoM2*, n=6, **D**) mice (Tm at P0). **(E)** Quantification of the total number of GFP+ cells in each layer (as indicated in **B**) of P8 mice. **(F–I)** H&E on cerebellar midsagittal sections at P30 mice. **(J)** Graph of the area of 3 midsagital cerebellar sections of Non-IR (n=3, circle) and IR (n=4, triangle) *Nes-GFP* (black) and *Nes-Smo* CKO (red) mice at P30. **(K)** Graph of the area of midsagital cerebellar sections at several developmental time points of *Nes-GFP* Non-IR (solid black; P4: n=3, P8: n=3 P12: n=4 and P30: n=3) and IR (dashed black; P4: n=3, P8: n=3, P12: n=3 and P30: n=4) and *Nes-Smo* CKO Non-IR (solid red; P4: n=3, P8: n=3, P12: n=3 and P30: n=3) and IR (dashed red; P4: n=3, P8: n=4, P12: n=4 and P30: n=4) mice. **(L)** Sample footprints (Forelimb in red and hindlimb in blue or black) from *Nes-GFP* Non-IR (solid black; n=5) and IR (dashed black; n=8) and *Nes-Smo* CKO Non-IR (solid red; n=5) and IR (dashed red; n=8) mice. **(M)** Graph showing changes in stride, sway and stance length. **(N)** Graph showing changes in the percentage of right (R) and left (L) difference between indicated conditions. **(O)** Graph showing the difference in latency to fall for each trial (red *: comparison between Non-IR and IR *Nes-Smo* CKO and black *: comparison between Non-IR and IR *Nes-GFP)* or total of mice between the different conditions. All Graphical data are presented as means ± SEM and significance was determined with two-

tailed Student's *t* test, **P*<*0.05*, ***P*<0.01, ****P*<0.001, *****P*<*0.0001*. Statistics are provided in Supp. Table 1. Scale bars in **B–D** indicate 100μm. Scale bars in **F–I** indicate 500μm.